

University of Groningen

Advanced receivers for submillimeter and far infrared astronomy

Kooi, Jacob Willem

IMPORTANT NOTE: You are advised to consult the publisher's version (publisher's PDF) if you wish to cite from it. Please check the document version below.

Document Version

Publisher's PDF, also known as Version of record

Publication date:

2008

[Link to publication in University of Groningen/UMCG research database](#)

Citation for published version (APA):

Kooi, J. W. (2008). *Advanced receivers for submillimeter and far infrared astronomy*. [Thesis fully internal (DIV), University of Groningen]. [s.n.].

Copyright

Other than for strictly personal use, it is not permitted to download or to forward/distribute the text or part of it without the consent of the author(s) and/or copyright holder(s), unless the work is under an open content license (like Creative Commons).

The publication may also be distributed here under the terms of Article 25fa of the Dutch Copyright Act, indicated by the "Taverne" license. More information can be found on the University of Groningen website: <https://www.rug.nl/library/open-access/self-archiving-pure/taverne-amendment>.

Take-down policy

If you believe that this document breaches copyright please contact us providing details, and we will remove access to the work immediately and investigate your claim.

Downloaded from the University of Groningen/UMCG research database (Pure): <http://www.rug.nl/research/portal>. For technical reasons the number of authors shown on this cover page is limited to 10 maximum.

Appendix A

The Allan variance method*

A.1 Introduction

There is a strong interest in the submillimeter astronomy community to increase the IF bandwidth of SIS receivers in order to better facilitate broad spectral linewidth and continuum observations of extragalactic sources. However, with an increase in IF bandwidth there is a decrease in the mixer total power stability. This in turn effects the integration efficiency and the quality of the measurement. In order to better understand the noise mechanisms responsible for reducing the receiver stability, we employ a technique first described by D.W. Allan and later elaborated upon by Schieder *et. al.*

Radio astronomy receivers in general look at very weak signals deeply embedded in noise. To extract the weak signals, synchronous detection (“signal on” - “signal off”) is typically employed. This is done by either slewing the entire telescope back and forth so as to get the beam on/off the source, or by nutating the secondary mirror (subreflector) of the telescope at a relatively fast rate. The problem in both these cases is the dead time between observations, i.e., chopping efficiency (η_c). A practical lower limit for slewing the whole telescope is typically 15 s, while chopping the secondary mirror can perhaps be as fast as 0.2 s (5 Hz). Frequency switching is possible and can be accomplished at a much higher rate. It suffers however from modulation of the LO-mixer standing wave (Chap. 10) [1], local oscillator power stability, and for terrestrial observations changes in the atmospheric transmission. For the high resolution Heterodyne Instrument (HIFI) on ESA’s Herschel satellite [2, 3] frequency switching is baselined as one of the observation modes.

If the noise in the receiver system is completely uncorrelated (white), it turns out that the rate of chopping (modulation frequency) has no effect on the final signal to noise ratio. This can be deduced from the well known radiometer equation (A.1) which

*The material described in this Appendix has been published in the following paper: J. W. Kooi, G. Chattopadhyay, M. Thielman, T. G. Phillips, and R. Schieder, in *Int. J. IR and MM Waves*, Vol. 21 (5) (2000).

states that uncorrelated noise with a Gaussian like spectral distribution integrates down with the square root of integration time

$$\sigma = \frac{\langle x(t) \rangle}{\sqrt{(\Delta\nu * T)}} . \quad (\text{A.1})$$

Here σ is the standard deviation (rms voltage) of the signal, $\langle x(t) \rangle$ the signal mean, $\Delta\nu$ the effective fluctuation bandwidth, and T is the total integration time of the data set.

In practice however, the noise in radiometers, and in particular SIS and HEB mixers, appears to be a combination of low frequency drift (correlated noise), $1/f$ electronic noise and white (uncorrelated) noise. Hence, there is an optimum integration time, known as the Allan stability time (T_A), after which observing efficiency is lost. In actual synchronous detection measurements n samples of difference data (“signal on” - “signal off”) are taken, each with a period T . These differences are then averaged so that the total observed time equals $n * (2T)$. If the period T is larger than the Allan stability time (T_A) of the system, then apart from loss in integration efficiency, there will be a problem with proper baseline subtraction. This manifests itself in baseline ripples at the output of the spectrometer which limits how well the noise integrates down with time (Sec. 2.3.5).

A.2 Theoretical considerations

To optimize observation efficiency, it is important to find the best secondary mirror (subreflector) chopping rate. This requires a knowledge of the nature of the receiver noise fluctuations. In practice, we employ a method developed by Allan [4], Barnes [5], and further elaborated on by Schieder *et al.* [6, 7].

Following Schieder’s analysis of synchronous detection, two sets of contiguous data samples are taking, each with the same integration time (T). The first measurement is the “on-source” signal $s(t)$, and the second measurement the “off-source” reference $r(t)$. In the analysis, it is assumed that there is no dead time between the data samples. If we define the first measurement as the integrated signal $s(t)$ over a period T

$$s(T) = \int_0^T s(t) dt , \quad (\text{A.2})$$

and the second measurement as:

$$r(T) = \int_T^{2T} r(t) dt , \quad (\text{A.3})$$

than difference of the two measurements is

$$d(T) = s(T) - r(T) . \quad (\text{A.4})$$

If μ is defined as the mean of $d(T)$, and σ^2 the variance of $d(T)$ then

$$\sigma^2(T) = \langle (d(T) - \mu)^2 \rangle = \langle d(T)^2 \rangle - \langle d(T) \rangle^2 . \quad (\text{A.5})$$

Here $\langle d(T)^2 \rangle$ is the mean (expectation value) of the difference squared and $\langle d(T) \rangle^2$ the squared mean of the difference. From [4] we find the Allan variance defined as

$$\sigma_A^2(T) = \sigma^2(T)/2 , \quad (\text{A.6})$$

so that

$$\sigma_A^2(T) = \frac{1}{2} \langle (d(T) - \langle d(T) \rangle)^2 \rangle . \quad (\text{A.7})$$

Because we look in astronomy at signals deeply embedded in the noise and are only interested in how the noise integrates down with time, we can make the simplification that there is essentially no signal present in $s(t)$. This means that the average of $d(T) = \langle d(T) \rangle = 0$, and we have under this condition the special situation that

$$\sigma_A^2(T) = \frac{1}{2} \langle d(T)^2 \rangle . \quad (\text{A.8})$$

Since in practice the data is only available in discrete form, we can use the more general expression of Eq. A.7 for a spectrometer channel k with fluctuation bandwidth $\Delta\nu$ as

$$\sigma_{A,k}^2(T) = \frac{1}{2(N-1)} \sum_{n=1}^N (d_k(n) - \langle d_k \rangle)^2 , \quad \langle d_k \rangle = \frac{1}{N} \sum_{n=1}^N d_k(n) . \quad (\text{A.9})$$

N equals the number of discrete time samples taken. Thus for a spectrometer with K channels, the average Allan variance spectrum (Fig. A.1b) can then be obtained by summing the variance of each individual channel, e.g.

$$\sigma_A^2(T) = \frac{1}{K} \sum_{k=1}^K \sigma_{A,k}^2(T) \quad (\text{A.10})$$

Other weightings are possible, for this we refer to Ossenkopf *et al.* [8].

The mathematical treatment of Eq. A.6 can be found in [5] for different types of noise spectra. If the noise spectral density is represented by a power law, then

$$S(f) = f^{-\alpha}, \quad \alpha = [1, 3] \quad (\text{A.11})$$

and one finds that

$$\sigma_A^2(T) \propto T^{\alpha-1} . \quad (\text{A.12})$$

$\alpha = 0$ stands for the white (uncorrelated) noise part of the spectrum, e.g.

$$\sigma_A^2(T) = \frac{\langle s(t) \rangle^2}{2\Delta\nu T} , \quad (\text{A.13})$$

$\alpha = 1$ for $1/f$ noise, and $\alpha \geq 2$ for correlated low frequency (drift) noise. Using a simple power law to characterize low frequency drift noise might not be correct however. A more accurate representation would be to describe the noise by a correlation function

$$g(\tau) = \langle r(t) * r(t + \tau) \rangle . \quad (\text{A.14})$$

The Allan variance can then be expressed as:

$$\sigma_A^2(T) = \frac{1}{T^2} \int_{-T}^T (T - |\tau|)(g(\tau) - g(T + \tau)) d\tau . \quad (\text{A.15})$$

Because we are interested only in integration times less than the correlated (drift) noise time scale, the correlation function can be expanded in a power series with only a few terms:

$$g(\tau) = g(0) - a\tau^\beta \pm \dots , \quad \beta = 1, 2, \dots \quad (\text{A.16})$$

From equation (A.15) we obtain

$$\sigma_A^2(T) \propto T^\beta . \quad (\text{A.17})$$

Combining equation (A.12) and equation (A.17) we find that for a noise spectrum that contains drift, white noise, and $1/f$ noise that the Allan variance takes the form

$$\sigma_A^2(T) = aT^\beta + \frac{b}{T} + c , \quad (\text{A.18})$$

where a, b , and c are appropriate constants and $\beta = \alpha - 1$. For short integration times, the variance decreases as $\frac{1}{T}$, as expected from the radiometer equation (A.1). For longer integration times, the drift will dominate as shown by the term aT^β . In that case, the variance starts to increase with a slope β which is experimentally found to be between 1 and 2. For SIS and HEB mixers it is frequently observed that the variance plateaus after some time T . This is attributed to the constant c and is representative of flicker or $1/f$ noise in the device under test.

Plotting $\sigma_A^2(T)$ on a log-log plot demonstrates the usefulness of this approach in analyzing the radiometer noise statistics (Fig. A.1b). As a reference it is meaningful to superimpose radiometric noise with a T^{-1} slope. The latter represents the uncorrelated (white) noise part of the spectrum. The minima in the plot gives the Allan time (T_A), the crossover from white noise to $1/f$ or drift noise. Often however, there is no clear minima, and a factor $\sqrt{2}$ deviation from the rms radiometric noise is then a useful definition of the Allan time. For the sake of optimum integration efficiency, one is advised to keep the integration time well below the system Allan time (Sec. 2.3.5).

Finally, it is often of interest to estimate what happens to the Allan stability time if spectrometer channels are binned to reduce the rms noise in an observed spectrum, or if the IF bandwidth of the radiometer is increased. Solving equation (A.18) for T as a function of receiver binned IF bandwidth $\Delta\nu'$ we get

$$T'_A/T_A = (\Delta\nu/\Delta\nu')^{\frac{1}{\beta+1}}. \quad (\text{A.19})$$

β the slope of the drift noise as discussed above. When the uncorrelated (white) noise component of the mixer spectral output power is reduced (by for example binning of spectrometer channels), the intersect between radiometric (A.1) and drift noise (A.17) occurs at an earlier time. Where exactly the two curves intersect depends on the statistical nature of the long term drift.

A.3 Total Power Allan variance

As an example we show in Fig. A.1 the time series and total power Allan variance (also known as the continuum Allan variance) of HIFI HEB mixer band 6a (H-polarization) as measured during the instrument level test phase (ILT) in May 2007. As we shall see, this plot contains a wealth of information. The IF output frequency of the HEB mixer is 2.4 – 4.8 GHz [9], which after being up-converted, and then back down-converted to match the 4 – 8 GHz wideband acousto-optical spectrometer (WBS) [10] input, translates to AOS subband1 (4.8 – 3.8 GHz), subband2 (3.8 – 2.8 GHz), and subband3 (2.8 – 2.4 GHz). “Full” corresponds to the total 2.4 GHz available HEB IF bandwidth. The left panel of Fig. A.1 depicts the averaged normalized time series of the full, and the three individual spectrometer subbands. It should be noted that the HEB mixer is most sensitive in the 2.4 – 3.4 GHz IF frequency range (Chap. 6) [9], and as a results it may be expected that WBS subband 3 is the most unstable. This is indeed the case as is evident from the top curve in Fig. A.1b. The offsets between the three spectrometer subband Allan times are due to excess noise in each of the IF subchannels. Averaged over the entire IF bandwidth, the calculated fluctuation

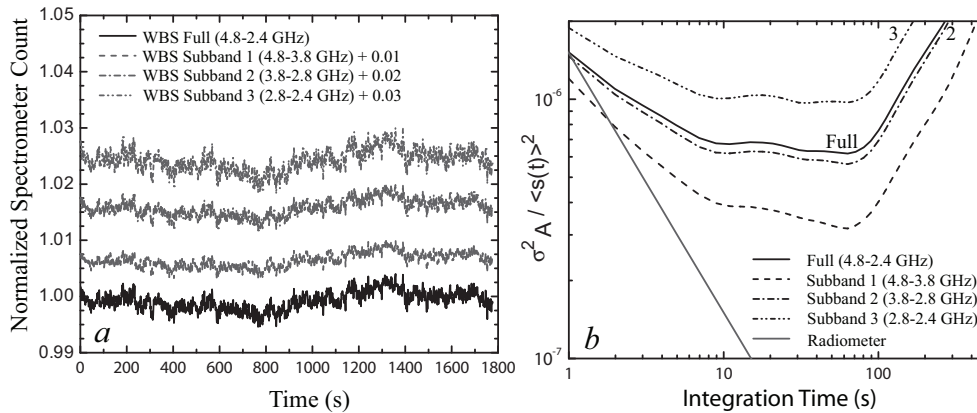


Figure A.1: *Left*) Time series for HIFI B6a HEB mixer, H-polarization, LO frequency = 1447 GHz. Curves have been offset for clarity. The statistical details of the noise are brought out by the Allan variance plot on the right. *Right*) The derived continuum, or total power Allan variance. The “full” (2.4 GHz) spectrometer response deviates a factor 2 from the radiometric noise at 3 s. This may be considered the effective total power “Allan variance minimum time” (T_A). See text for details.

noise bandwidth ($\Delta\nu$) is 1.3 MHz. This is somewhat less than the spectrometer [10] intrinsic noise bandwidth of 2.3 MHz, indicative of some excess (non-radiometric) noise.

Again referring to Fig. A.1b, we see that the noise integrates down with a slope slightly less than $(\Delta\nu T)^{-1}$ between 1 s and 7 s. Judging from the -1 radiometer slope, we have a factor 2 loss in integration efficiency at ~ 3 s. This may be considered the effective ‘‘Allan minimum time’’. The reason that there is not a clear minimum in the Allan variance plot is that HEB mixers exhibit significant $1/f$ fluctuation noise (zero slope), in this case between ~ 10 s – 90 s. Above approximately 90 s, drift noise begins to dominate. In this particular example the drift slope $\beta = +1.2$. For a further discussion on this subject we refer to Chap. 10.

A.4 Spectroscopic Allan variance

The spectroscopic Allan variance measures deviations from the continuum level fluctuations [8]. As such it corresponds to the subtraction of the spectrometer mean continuum level, known as the zeroth order baseline correction, as proposed by Schieder, Ossenkopf, and Siebertz [7, 8, 11]. This is allowed since most heterodyne observations are intended for line observations, rather than continuum or flux calibration. For continuum observations incoherent detectors are better suited (Chap. 2). The spectroscopic normalization for two channels is given by Eq. 10.4. For K spectrometer channels the signal in each channel ($d_k(n)$) at time n may be normalized by subtraction of the instrument zero level in the particular channel (z_k), and then by dividing the difference by the temporal average of each channel

$$s'_k(n) = \frac{d_k(n) - z_k}{\langle d_k(n) - z_k \rangle_n}, \quad z_k = \frac{1}{N} \sum_{n=1}^N d_k(n). \quad (\text{A.20})$$

To now obtain the difference for the spectroscopic Allan variance computation, we subtract the normalized mean summed over all spectrometer channels of interest, e.g.

$$s_k(n) = s'_k(n) - \langle s'_k(n) \rangle_k. \quad (\text{A.21})$$

$s_k(n)$ may then be substituted for $d_k(n)$ in Eq. A.9 to obtain the spectroscopic Allan variance for each channel.

In Fig. A.2a we show the spectroscopic Allan variance. In this case a zeroth order correlated noise baseline is subtracted. We see a substantial improvement in the statistical variance of the spectra. The noise now integrates down radiometrically, for about 50 s in case of the subbands, and 15 s for the full spectrometer band (4.8 – 3.8 GHz). The $1/f$ gain fluctuation noise that dominates the continuum Allan variance of Fig. A.1b has been nearly completely removed! Taking the ratio of the spectroscopic to the total power Allan variance (Fig. A.2b), we find that statistically the largest improvement (factor 10+) is gained by spectrometer subband 3 at integration times > 10 s. This is good news as most galactic (narrow line) observations will be planned in this subband, being the most sensitive region of the HEB IF passband [9].

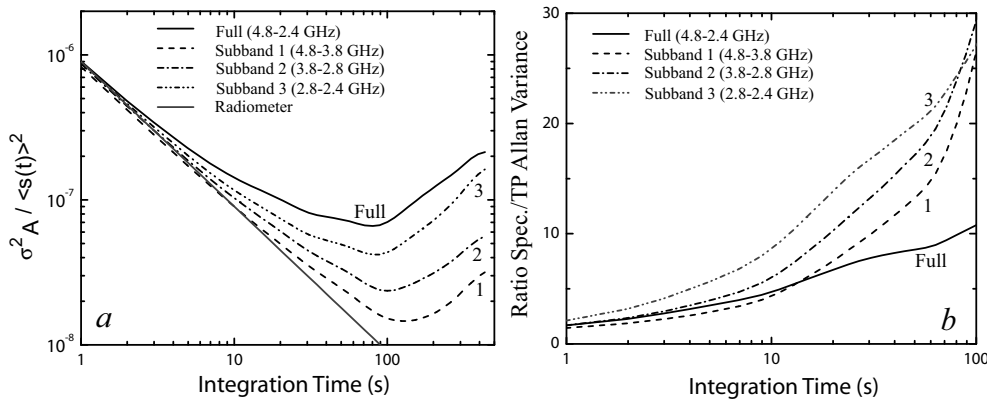


Figure A.2: *Left*) Spectroscopic Allan variance for the B6a HEB mixer subbands and full spectrometer band (2.4 GHz). The Allan times, defined as a factor of two deviation from the radiometric noise (white) are: $T_A(\text{full})=14.9$ s, $T_A(\text{subband1})=111$ s, $T_A(\text{subband2})=50.5$ s, and $T_A(\text{subband3})=30.7$ s. The noise fluctuation bandwidth is 2.3 MHz. *Right*) Ratio of the spectroscopic to the total power (Fig A.1b) Allan variance. Not surprising, the greatest improvement is obtained at long integration times. Spectrometer subband 3 offers the greatest improvement, as it constitutes only 400 MHz of bandwidth and is the most unstable (highest sensitivity) to start out with. H-polarization for the mixer band, LO frequency = 1447 GHz

For spectral line broadened extragalactic observations the full spectrometer will need to be used in which case a factor six improvement over the continuum stability is obtained.

It should be noted that the HIFI B6a results presented here serve as an example of system stability. Actual HEB mixer stability (Chap. 10) [1] may be better in a more optimized environment such as space, or possibly worse in a poorly designed ground based application. The balanced approach of Chap. 8, by virtue of reduced sensitivity to local oscillator amplitude noise, is expected to improve the HEB mixer system stability.

A.5 Improvement of spectroscopic over total power Allan variance

To further compare the improvement in spectroscopic Allan variance over continuum Allan variance, we compare in Fig. A.3 the ratios of HIFI SIS band 2 (736 GHz) and HEB mixer band 6 (1652 GHz). For the HEB mixer, subband 1 has the lowest sensitivity (4.4 – 4.8 GHz), and also shows the least improvement. The loss in sensitivity of an HEB mixer is caused by the roll of in mixer gain, as described in Sec. 6.5, overlaid by the frequency response of the diplexer used to inject the LO signal. For the band 2 SIS mixer the sensitivity is uniform across all spectrometer subbands. In this case a beam splitter is used to inject the LO signal. Why the spectroscopic-over continuum Allan variance ratio is not more uniform is not entirely clear, except to note that the 7 – 8 GHz IF channel (subband 4) has always the worst stability

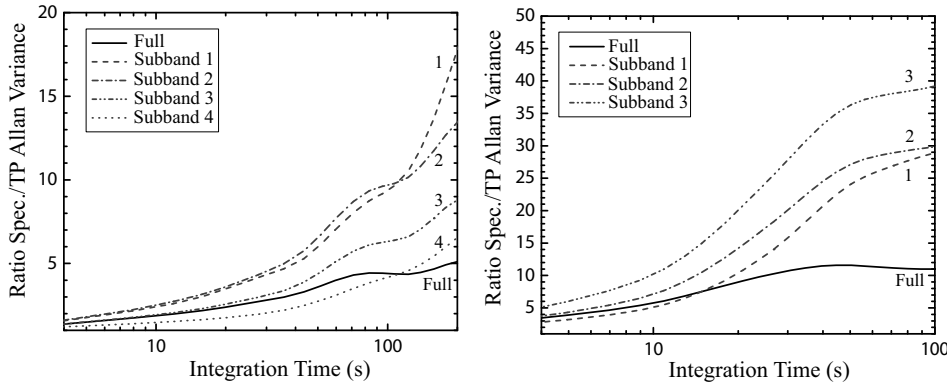


Figure A.3: *Left*) Improvement ratio of the spectroscopic Allan variance for HIFI SIS mixer band 2b. LO frequency is 736 GHz. *Right*) Improvement ratio of the spectroscopic Allan variance for HIFI HEB mixer band 6b. LO frequency is 1652 GHz. Note that the plots have different scales. The behavior of the individual subbands is noticeably different. The removal of a zeroth order baseline has significantly more effect on a per subband bases for an HEB mixer than SIS mixer. This indicates that the source of HEB instability (see also Chap. 10) is highly correlated in an HEB mixer. The most likely culprits are: LO instability and optical standing waves. SIS mixer band 2 is a beamsplitter band, and HEB mixer band 6 uses a diplexer to inject the LO signal. Due to the finite diplexer passband and roll of in mixer gain, HEB subband 1 has considerably lower sensitivity than subband 3. For both mixer bands, we have plotted the vertically polarized IF output channel.

performance. It is likely that we see an additive effect of the many subcomponents in the IF- and backend system. In general it appears therefore that the noise of a SIS mixer is less correlated in the higher end of the IF band.

Significantly, a greater amount of spectroscopic- over continuum Allan variance improvement is obtained in the HEB mixer band than the SIS mixer band. There are several explanations for this. First, as we have seen in Sec. 4.3, the HEB is a power sensor. This is opposed to a SIS junction that is sensitive to quasi-particle tunneling through a thin barrier (Sec. 4.1). Second, HEB mixers operate in the terahertz frequency regime. As such they are more sensitive to optical standing waves than SIS mixers, which primarily operate below 1 THz. This is the subject of Sec. 10.3.2. And finally, the LO sources that pump the mixers are more complex at higher operating frequencies (HEB mixers), and thus more susceptible to amplitude noise which increases approximately as $20\log_{10}(N^2)$ [12]. N is the local oscillator multiplication factor. Hence the argument that a balanced HEB mixer configuration is liable to have improved system stability performance.

Bibliography

- [1] J. W. Kooi, J. J. A. Baselmans, A. Baryshev, R. Schieder, M. Hajenius, J. R. Gao, T. M. Klapwijk, B. Voronov, and G. Gol'tsman, "Stability of Heterodyne Terahertz Receivers", *Journal of Applied Physics*, Vol. 100, 064904, Sep. (2006).
- [2] Th. de Graauw, N. Whyborn, E. Caux, T. G. Phillips, J. Stutzki, X. Tielens, R. Güsten, F. P. Helmich, W. Luinge, J. Pearson, P. Roelfsema, R. Schieder, K. Wildeman, and K. Wavelbakker, "The Herschel-Heterodyne Instrument for the Far-Infrared (HIFI)", [Online]. Available: herschel.esac.esa.int/Publ/2006/SPIE2006_HIFI_paper.pdf
- [3] [Online]. Available: Herschel; <http://sci.esa.int/>
- [4] D. W. Allan, "Statistics of Atomic Frequency Standards", *Proc. IEEE*, Vol. 54, No. 2, pp 221-230, (1969).
- [5] A.B Barnes, "Characterization of frequency stability", *IEEE Trans. Instrument Measurements*, Vol. IM-20, no. 2, pp. 105-120, (1971).
- [6] R. Schieder, "Characterization and Measurement of System Stability", *SPIE*, Vol 598, Instrumentation for Submillimeter Spectroscopy (1985).
- [7] R. Schieder and C. Kramer, "Optimization of Heterodyne Observations using Allan variance Measurements", *Astron. Astrophys.*, Vol. 373, 746-756 (2001).
- [8] V. Ossenkopf, "The stability of spectroscopic instruments: A unified Allan variance computation scheme", *A & A*, Vol. 479, 915-926 (2008).
- [9] A. Cherednichenko, V. Drakinskiy, T. berg, P. Khosropanah, and E. Kollberg, "Hot-electron bolometer terahertz mixers for the Herschel Space Observatory", *Rev. Sci. Instrum.*, Vol. 79, 034501, (2008).
- [10] R.Schieder, O. Siebertz, F. Schloeder, C. Gal, J. Stutzki, P. Hartogh, and V. Natale, "Wide-Band Spectrometer for HIFI-FIRST", *Proc. of "UV, Optical, and IR Space Telescopes and Instruments"*, J. B. Breckinridge, P. Jakobsen Eds., SPIE 4013, 313-324, Jul., (2000).
- [11] O. Siebertz, "Akusto-optisches Spektrometer mit variabler Auflösung", PhD thesis, University Cologne, (1998).

- [12] N. Erickson, "AM Noise in Drives for Frequency Multiplied Local Oscillators", *Proc. 15th Int. Symp. on Space Terahertz technology*, Northampton, MA, (2004), pp. 135-142.

Appendix B

Transmission properties of Zitex*

B.1 Introduction

Advances in submillimeter SIS receivers necessitate the use of very-low-loss components in order to achieve theoretical performance. Often these optical elements are cooled to 4 K, where their properties are less well measured. The advanced SIS receivers of Chaps. 7–9 achieve noise temperatures as low as 3–5 times the quantum noise limit ($h\nu/k_B$), of which up to 30 % may stem from optical loss. Modern bolometric instruments have comparable optical efficiencies. Clearly, choosing materials with optimum dielectric constants, low absorption loss and optimal cryogenic performance is very important.

To reduce the loading on cold optical elements operating in the far-infrared, room temperature infrared radiation must be blocked efficiently while allowing the desired wavelengths to pass unattenuated [1, 2]. Quartz is a low-loss material when a suitable antireflection coating like Teflon is applied, but this is difficult and restricts the wavelengths over which it can be used as a highly transmissive element [3]. Teflon itself is a good IR block, but transmits power in the 5–10 μm range and longward of 50 μm , limiting its usefulness. Several more absorbing materials, such as Fluorogold and Fluorosint, have been used for low frequency applications, but their slow spectral cut-off characteristics are not ideal for receivers operating above ~ 400 GHz [3, 4].

With this in mind we have measured (Table B.1) the power absorption coefficient, refractive index, and thermal conductivity of Zitex at 290 K, 77 K, and 4 K in the 1 to 1000 μm spectral range. This was accomplished with the use of three Fourier Transform Spectrometers (FTS) [5]. Zitex [6] is a sintered Teflon material with voids of 1–60 μm and a filling factor of 50 %. Several different varieties are available, divided

*A subsection of the material described in this Appendix has been published in the following paper: D. J. benford, M. C. Gaidis, and J. W. Kooi, *Proc. 10th Int. Symp. Space Terahertz Technology*, (1999), pp. 402 ff.

Table B.1: Zitex samples measured.

Grade	Pore Size (μm)	Thickness (mm)	Filling Factor [†]	NIR data	FIR data	Submm data
G104	5–6	0.10	0.45	✓		
G106	4–5	0.16	0.50	✓		
G108	3–4	0.20	0.55	✓	✓	
G110	1–2	0.25	0.60	✓	✓	
G115	1–2	0.41	0.60	✓		
G125	~3	3.53	~0.5	✓		✓
A155	2–5	0.27	0.40	✓		

[†] Relative density of Teflon.

into two categories by manufacturing process. Zitex A is designed to reproduce filter paper. It has many narrow linear paths through it and is a rough but soft sheet. It is available in 11 grades with effective pore sizes ranging from 3 μm to 45 μm and in thicknesses from 0.13 mm (0.005”) to 0.64 mm (0.025”). Zitex G is made of sintered Teflon spheres of small sizes, resulting in a denser, smoother material. Available in 5 grades, the pore sizes range from 1.5 μm to 5.5 μm and is available in standard thicknesses of 0.10 mm (0.004”) to 0.38 mm (0.015”), although larger thicknesses are available.

Zitex is similar in geometry to glass bead filters, in which dielectric spheres are embedded in a suspending material with a different index of refraction. A single sphere of radius a in a material of index n will scatter strongly for wavelengths $\lambda \lesssim \pi a(n-1)$ [7]. Thus, for Teflon ($n = 1.44$ [8]), a sphere of radius 10 μm produces a shadow for wavelengths shortward of 15 μm . At short wavelengths a perfectly randomly scattering screen will redistribute the optical power in an incident beam equally in all directions, resulting in a large loss for well-collimated beams.

Zitex is an effective IR block, with thin (200 μm) sheets transmitting less than 1 % in the 1–50 μm range while absorbing $\lesssim 10$ % at wavelengths longer than 200 μm . Some variation in the cutoff wavelength is seen, tending to be a shorter wavelength cutoff for a smaller pore size. In addition, the thermal conductivity of Zitex at cryogenic temperatures has been measured, and is found roughly one-half that of bulk Teflon.

B.2 Zitex G104, G106, G108, G110, G115, & A155

The samples of G104 and G106 were measured in the near- to mid-infrared to derive a transmission and an effective absorption coefficient, as shown in Fig. B.1. The absorption coefficient α for a sheet of thickness d is calculated from the transmission t_{rf} as $-\ln(t_{rf})/d$. Since some wavelength-dependent fraction of the loss ($1 - t_{rf}$) is

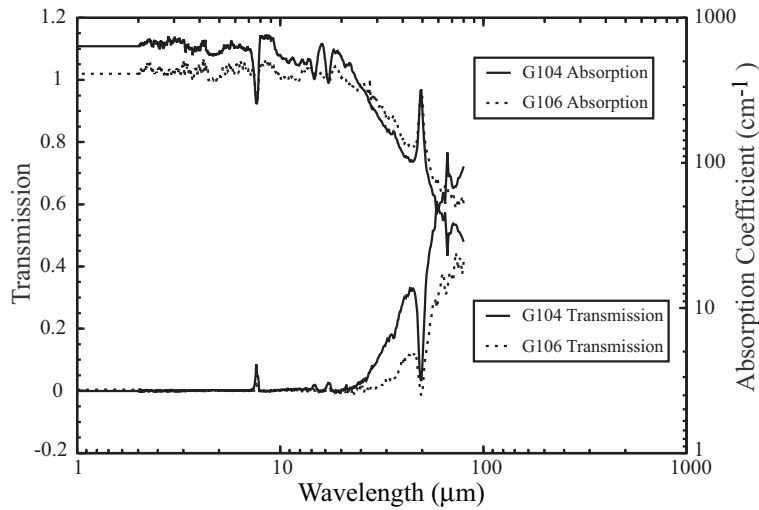


Figure B.1: Transmission and effective absorption coefficient in nepers per cm of single sheets of Zitex G104 and G106 (pore sizes 5–6 μm and 4–5 μm , respectively).

from scattering and some from absorption, the absorption coefficient cannot be used to estimate the transmission of arbitrary thicknesses. It does, however, provide a useful means of comparison with other, more purely absorptive, materials.

Combining sets of data in the near- through far-infrared for samples of G108 and G110 allows to build a more complete picture of the turn-on profile of Zitex near 100 μm , as shown in Fig. B.2.

B.3 Multiple Layers

A LHe-cooled receiver is likely to have several layers of infrared-blocking filtration in the optical path. As a result, it is natural in the case of a scattering material like Zitex to question its efficiency in a multilayer application. Layering single-, double-, and triple sheets of Zitex in close proximity (limited only by the natural wavy contours of the thin sheets) shows that scattering is the dominant loss mechanism and that multiple sheets are not substantially more effective than single sheets [5].

Using Zitex A155 sheets spaced by roughly 7 mm, we find the transmission shown in Fig. B.3. At mid-infrared wavelengths, the Zitex still appears to be dominated by scattering since the effective absorption coefficient of two layers is less than that for of one layer. However, at far-infrared wavelengths, the transmission appears to be increasingly determined by absorption alone, presumably in the bulk of the Teflon; the absorption is similar to that of Birch [9].

B.4 Temperature Variation

For many materials (e.g., quartz), the absorption of mid-infrared radiation is known to vary as the temperature changes [10]. To determine if there was any effect of the

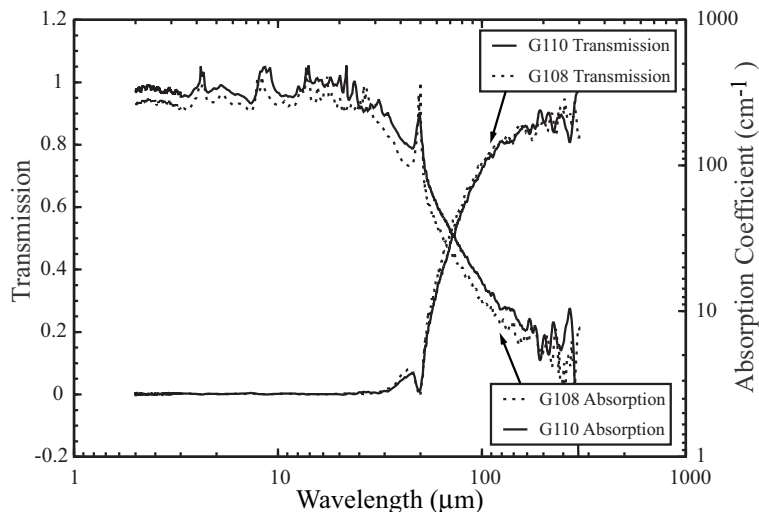


Figure B.2: Transmission and effective absorption coefficient in nepers per cm of single sheets of Zitex G108 and G110 (pore sizes 3–4 μm and 1–2 μm , respectively) using near-, mid-, and far-infrared data.

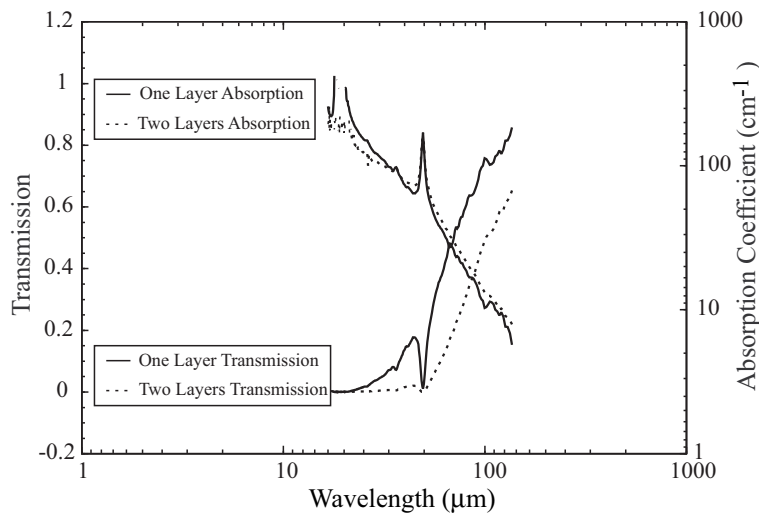


Figure B.3: Transmission of single and double layers of Zitex in an $f/4$ beam with ~ 7 mm spacing. At mid-IR wavelengths, the Zitex acts as two scattering surfaces; at far-IR wavelengths, like an absorber. Adding 7 mm of space between the layers extends the turn-on to longer wavelength.

temperature on the transmission of Zitex, we measured the transmission of samples of G110 at 300 K and 77 K in the far-infrared near the turn-on region. No significant variation in the transmission was seen upon cooling which is to be expected for dielectric scattering.

B.5 Refractive Index

Measuring the refractive index of a material of low dielectric constant is difficult near 1 THz for a nondispersive FTS. Only the thick sample of G125 could be measured, via a determination of the fringe spacing in the 3.5 mm thick slab. The fringe spacing, averaged between 13 and 45 cm^{-1} (200 – 800 μm or 400 – 1350 GHz), was 1.18 cm^{-1} . This provides a refractive index for Zitex of $n = 1.20 \pm 0.07$ at a temperature of 2 K. This can be compared to Teflon, which has $n = 1.44$ [8]; with a filling factor of $\sim 50\%$, the expected refractive index is $n = 1.22$, exactly as measured.

B.6 Thermal Conductivity

The thermal conductance of a thick slab of Zitex was measured in the direction along the sheet using an apparatus developed for the purpose of measuring lateral thermal conductance in sheets [11]. At cryogenic temperatures ($T \leq 150$ K), the conductivity of Zitex is found well fit by $K(T) = 0.01 T^{0.58} \text{ W K}^{-1}\text{m}^{-1}$. This value is half the bulk conductivity of Teflon [12], indicating that the porous nature of Zitex does not substantially affect its thermal conductance beyond the geometric reduction.

However, since Zitex sheets tend to be thin (~ 0.3 mm), even the small power incident on Zitex when used as a near-infrared blocking filter will raise its temperature by a significant fraction. This suggests the use of two layers for good blocking, whereas one Teflon layer might have been sufficient to handle the optical loading. Since the loss in Zitex at long wavelengths is so low however, the two layer solution is likely to be more efficient than the use of solid Teflon.

Bibliography

- [1] J. W. Kooi, M. Chan, B. Bumble, H. G. Leduc, P.L. Schaffer, and T. G. Phillips, “230 and 492 GHz Low-Noise SIS Waveguide Receivers employing tuned Nb/AlO_x/Nb tunnel junctions”, *Int. J. IR and MM Waves*, Vol. 16, No. 12, pp. 2049-2068, Dec. (1995).
- [2] T. R. Hunter, D. J. Benford, and E. Serabyn, “Optical Design of the Submillimeter High Angular Resolution Camera (SHARC)”, *PASP*, Vol. 108, p. 1042 (1996).
- [3] D. J. Benford, J. W. Kooi, and E. Serabyn, “Spectroscopic Measurements of Optical Components Around 1 Terahertz”, *Proc. 9th Int. Symp. on Space Terahertz Technology*, p. 405 (1998).
- [4] J. W. Lamb, “Miscellaneous Data on Materials for Millimetre and Submillimetre Optics”, *Int. J. IR MM Waves*, Vol. 17, no. 12, pp. 1997–2034 (1996).
- [5] D. J. benford, M. C. Gaidis, and J. W. Kooi, “Transmission Properties of ZITEX in IR-Submm”, *Proc. 10th Int. Symp. Space Terahertz Technology*, (1999), pp. 402ff.
- [6] Norton Performance Plastics, Wayne, New Jersey. (201) 696-4700.
- [7] S. Sato, S. Hayakawa, T., Matsumoto, H. Matsuo, H. Murakami, K. Sakai, A. E. Lange and P. L. Richards, “Submillimeter wave low pass filters made of glass beads”, *Applied Optics*, Vol. 28, no. 20, p. 4478 (1989).
- [8] J. Kawamura, S. Paine, and D. C. Papa, “Spectroscopic Measurements of Optical elements for Submillimeter Receivers”, *Proc. 7th Int. Symp. on Space Terahertz Technology*, pp. 349 (1996).
- [9] J. R. Birch, “The Far-Infrared Optical Constants of Polypropylene, PTFE, and Polystyrene”, *Infrared Phys.*, Vol. 6, no. 1, pp. 33–38 (1992).
- [10] F. Bréhat and B. Wyncke, “Measurements of the Optical Constants of Crystal Quartz at 10K and 300K in the Far Infrared Spectral Range: 10-600 cm⁻¹”, *Int. J. IR MM Waves*, Vol. 18, no. 9, pp. 1663–1679 (1997).
- [11] D. J. Benford, T. J. Powers, and S. H. Moseley, “Thermal Conductivity of Kapton Tape”, *Cryogenics*, Vol. 39, no. 1, pp. 93–95 (1999).

- [12] G. E. Childs, L. J. Ericks, and R. L. Powell, "Thermal Conductivity of Solids at Room Temperature and Below", *NIST-NBS Monograph #131*, (1973).

Appendix C

AR coated HDPE windows*

C.1 Introduction

Pressure windows, infrared blocking filters, and lenses are by definition made of dielectric materials with refractive indexes > 1 (vacuum). Aside from absorption loss (Sec. 4.2.2), dielectric materials used in the above described manner also suffer from reflection loss at the interface to free space. Before addressing this issue, it is instructive to look at a dielectric slab from an optical engineering perspective. As was seen in Sec. 10.3.2, the fractional transmitted power in a cavity (voltage standing wave inside the dielectric slab) can be described by an Airy function

$$A_i(\nu) = \frac{1}{1 + F \sin^2(\frac{\delta}{2})}, \quad \delta = \frac{4\pi nd}{\lambda_0}. \quad (\text{C.1})$$

n is the refractive index of the material, d the thickness of the dielectric slab, λ_0 the free space wavelength, and F the finesse

$$F = \frac{4|r|^2}{(1 - |r|^2)^2}. \quad (\text{C.2})$$

For normal incidence, r the magnitude of the reflection is polarization independent and may be obtained from

$$|r_{\perp}| = \frac{n - 1}{n + 1}, \quad n = \sqrt{\epsilon_r}. \quad (\text{C.3})$$

The Airy function has a maximum value (no internal reflection) for $\delta = 0, 2\pi, 4\pi, \dots$, and a minimum for $\delta = \pi, 3\pi, \dots$.

Traditionally z-cut quartz is used for vacuum windows, and infrared-blocking filters, because of its high transparency in the submillimeter, relatively low dielectric

*A subsection of the material described in this Appendix has been published in the following paper: D. J. Benford, J. W. Kooi, and E. Serabyn, *Proc. 9th Int. Symp. on Space Terahertz Technology*, p. 405 (1998).

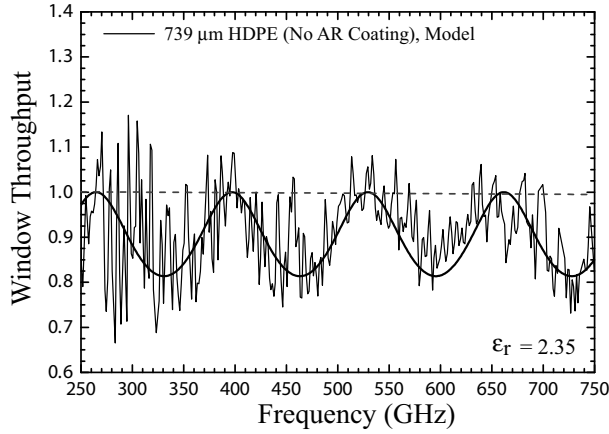


Figure C.1: Measured and modeled transmission of a $739 \mu\text{m}$ thick high-density polyethylene (HDPE) pressure window. From a fit against the model we obtain a dielectric constant $\epsilon_r = 2.35$. The increase in noise below 350 GHz is due to the decrease in the FTS bolometer responsivity.

constant ($\epsilon_r=3.8$), and opaqueness to helium and other gasses. However, the refractive index is high enough to cause substantial reflections loss. As an example, we find for quartz a maximum constructive interference amplitude ($1-Ai_{\text{quartz}}$) of 0.3403. This corresponds to a 34 % voltage reflection loss, which in power corresponds to a worst case scenario loss of 11.56 %. Of course this is only at one frequency, with the mean reflected power obtained from $r_{\perp}^2 \sim 10$ %.

To minimize reflection loss, antireflection coating of the dielectric slab's surface is frequently utilized. In the case of quartz, only Teflon has the ideal dielectric constant and required low loss tangent for appropriate antireflection material. Unfortunately, adhesion of Teflon to quartz is very difficult and therefore costly. This is especially so in the submillimeter where a quarter-wave antireflection coating requires substantial thickness. Other materials such as silicon ($\epsilon_r = 11.8$) with as antireflection coating Parylene-c [1] have been investigated. However the dielectric constant of Parylene-c ($\epsilon_r = 2.62$) and material absorption loss are not ideal, vacuum deposition is specialized, and signal bandwidth due to the high dielectric constant of silicon (Eq. C.1) limited. For this reason antireflection coated silicon windows/infrared blocks have seen limited application in the submillimeter frequency regime.

An interesting alternative to quartz is high-density polyethylene (HDPE). This material is used by many research groups to make lenses, infrared-blocking filters, and vacuum pressure windows. HDPE has good transmission well into the far infrared, good to excellent blockage of helium and other atmospheric gasses, and a low dielectric loss tangent (Eq. 4.84). To obtain the dielectric constant of HDPE we measured the transmission of a $739 \mu\text{m}$ thick slab on a Fourier transform Spectrometer (FTS). The result is shown in Fig. C.1.

Fitting our model to the measurement we derive a dielectric constant (ϵ_r) of 2.35. Given the thickness of the sample, we calculate (Eq. C.1) a signal (amplitude) transmission of 0.8415. This is in good agreement with the measurement.

C.2 Antireflection coating

Antireflection (AR) coating of the surface is generally best understood from an electrical circuit analysis point of view. Similar to Eq. 4.54, we can describe the input impedance of a general transmission line as

$$Z_s = Z_0 \frac{Z_l + iZ_0 \tan(\beta l)}{Z_0 + iZ_l \tan(\beta l)} = \frac{Z_l \cos(\beta l) + iZ_0 \sin(\beta l)}{Z_0 \cos(\beta l) + iZ_l \sin(\beta l)}. \quad (\text{C.4})$$

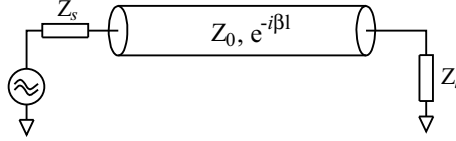


Figure C.2: General transmission line model of Eq. C.4.

β is the propagation constant $= 2\pi/\lambda$, Z_l the load impedance at the end of the transmission line (Z_{slab}), Z_s the input impedance of the transmission line which ideally equals the free space impedance $\eta_0 = 377 \Omega$ for minimum reflection, Z_0 is the impedance of the intermediate (antireflection) dielectric layer, and βl the electrical length. For $\beta l = \pi/2$ (or multiple thereof),

$$Z_s = \frac{Z_0^2}{Z_l} \rightarrow \eta_0 = \frac{Z_0^2}{Z_{slab}}, \quad (\text{C.5})$$

so that $Z_0 = \sqrt{\eta_0 Z_{slab}}$. The relative dielectric slab impedance normalized to the free space impedance is $Z_{slab}/\eta_0 = 1/\epsilon_r$. And thus we see that Z_0 , the antireflection layer impedance, relative to the dielectric slab equals $Z_{slab}/Z_0 = \sqrt{\epsilon_r}$. A quarter wavelength in the AR layer material is obtained for $d_{AR} = \lambda_0/4\sqrt{n}$, $n = \sqrt{\epsilon_r}$.

In Fig. C.3 we show a measurement and simulation of a 230 GHz Teflon AR coated quartz window (2.5 mm thick). The internal reflections (Fabry-Perot pattern) perfectly cancel at 230 GHz. At the edges of the band (180 GHz & 280 GHz), the voltage reflection loss has degraded $\sim 8\text{--}10\%$ (1% in power).

C.3 Multi-layer antireflection coating

To model (multi-layer) antireflection coatings, it is most convenient to express the transmission line with impedance Z_0 and electrical length γl as an ABCD matrix. γ is the complex propagation constant $\alpha + i\beta$ as in Eq. 4.77. In this way any number of layers can be build up by cascading the ABCD matrixes, similar to what is shown in Fig. C.4. The ABCD matrix of a transmission line can be described as a 2-port:

$$\begin{bmatrix} A & B \\ C & D \end{bmatrix} = \begin{bmatrix} \cosh(\gamma l) & Z_0 \sinh(\gamma l) \\ Y_0 \sinh(\gamma l) & \cosh(\gamma l) \end{bmatrix}. \quad (\text{C.6})$$

Cascading yields,

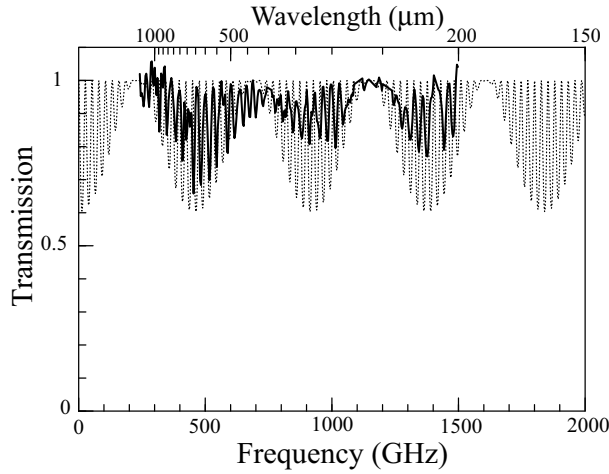


Figure C.3: Transmission of an antireflection coated quartz window designed for the 230 GHz region.

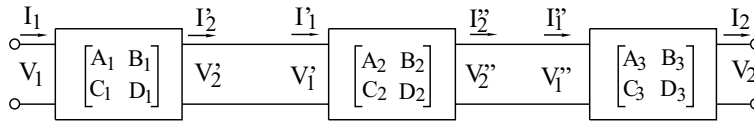
$$\begin{bmatrix} V_1 \\ I_1 \end{bmatrix} = \begin{bmatrix} A_1 & B_1 \\ C_1 & D_1 \end{bmatrix} \begin{bmatrix} A_2 & B_2 \\ C_2 & D_2 \end{bmatrix} \begin{bmatrix} A_3 & B_3 \\ C_3 & D_3 \end{bmatrix} \begin{bmatrix} V_2 \\ I_2 \end{bmatrix}. \quad (\text{C.7})$$

Multiplying the individual matrixes yields the overall ABCD matrix. The equivalent two-port S-parameter matrix can then be calculated [2]

$$\begin{bmatrix} S_{11} & S_{12} \\ S_{21} & S_{22} \end{bmatrix} = \begin{bmatrix} \frac{A+B/Z_s-CZ_s-D}{A+B/Z_s+CZ_s+D} & \frac{2(AD-BC)}{A+B/Z_s+CZ_s+D} \\ \frac{2}{A+B/Z_s+CZ_s+D} & \frac{-A+B/Z_s-CZ_s+D}{A+B/Z_s+CZ_s+D} \end{bmatrix}. \quad (\text{C.8})$$

The matrix will be reciprocal (no non-linear elements) so that $S_{11} = S_{22}$ and $S_{12} = S_{21}$. In this case S_{11} represents the input return loss (reflected power equals $20\log_{10}[S_{11}]$) and S_{21} the forward transmission (power transmission = $20\log_{10}[S_{21}]$).

To investigate the use of low cost infrared blocks and vacuum windows we have [3] antireflection coated HDPE with Zitex. Zitex, being 50 % porous Teflon has a melting point of $\sim 327^\circ\text{C}$, significantly higher than that of HDPE ($130\text{--}137^\circ\text{C}$). Using a thin ($25\text{--}50\ \mu\text{m}$) layer of low-density polyethylene (LDPE) [4] with a melting point $\sim 10^\circ\text{C}$



$$\begin{bmatrix} V_1 \\ I_1 \end{bmatrix} = \begin{bmatrix} A_1 & B_1 \\ C_1 & D_1 \end{bmatrix} \begin{bmatrix} V_2' \\ I_2' \end{bmatrix} \quad \begin{bmatrix} V_1' \\ I_1' \end{bmatrix} = \begin{bmatrix} A_2 & B_2 \\ C_2 & D_2 \end{bmatrix} \begin{bmatrix} V_2'' \\ I_2'' \end{bmatrix} \quad \begin{bmatrix} V_1'' \\ I_1'' \end{bmatrix} = \begin{bmatrix} A_3 & B_3 \\ C_3 & D_3 \end{bmatrix} \begin{bmatrix} V_2 \\ I_2 \end{bmatrix}$$

Figure C.4: Antireflection layers and dielectric slab modeled as a series of cascaded ABCD matrixes.

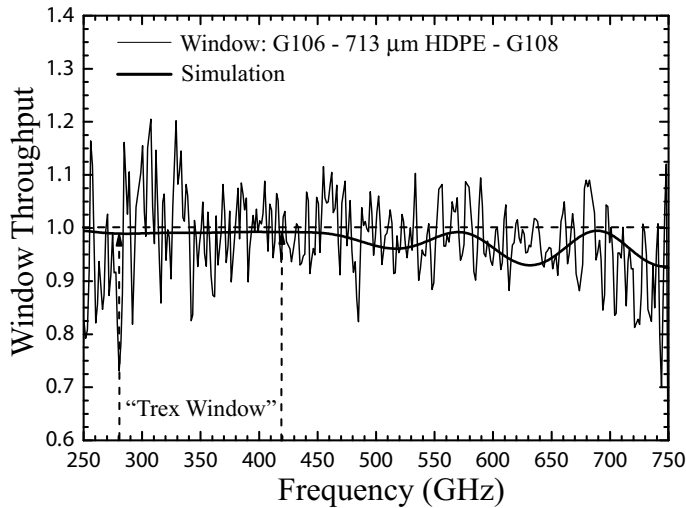


Figure C.5: Measured and modeled 713 μm HDPE window with G106 and G108 Zitex AR coating. This window is presently used on the “Technology Development Receiver” of Chap. 7. The expected reflection loss is on the order of 2 % (~ 6 K). Careful leak checks of the cryostat revealed no noticeable permeability to helium.

below that of HDPE as a glue, we have under pressure (1/4 ton) and heat (125°C) successfully fused a “sandwich” of Zitex-LDPE-HDPE-LDPE-Zitex.

To maximize the RF bandwidth while minimizing reflection, it was found through computer simulations [5] that the use of Zitex with different sheet thickness on either side of the HDPE window is preferred. In Fig. C.5 we show the measured and simulated response of a vacuum window made of 713 μm high-density polyethylene (HDPE), antireflection coated with a single layer (150 μm) G106 Zitex on one side, and a single layer (200 μm) G108 on the other side. The pressure window was designed to cover the 280 – 420 GHz technology receiver passband of Chap. 7. The calculated transmission is better than 98 % between 280 GHz – 420 GHz, with an input return loss < -20 dB. As is evident from the FTS measurement, the method works very well with the benefit of having essentially no cost associated with it!

As a final note, ALMA [6] has developed excellent five-layer quartz vacuum windows (Zitex-HDPE-quartz-HDPE-Zitex), albeit at a significant complexity and cost. The performance of the described Zitex-LDPE-HDPE-LDPE-Zitex “sandwich” is very competitive with these excellent multi-layer windows. Because the thinnest sheet of Zitex is 100 μm (G104), the application of the Zitex-LDPE-HDPE-LDPE-Zitex technique is limited to ~ 750 GHz. Above this frequency range, HDPE with antireflection grooves [7], quartz windows with suitable AR coated (Teflon), or possibly Parylene coated silicon windows will need to be utilized.

Bibliography

- [1] A. J. Gatesman, J. Waldman, M. Ji, C. Musante, and S. Yagvesson, “An antireflection coating for silicon optics at terahertz frequencies”, *IEEE Microwave and Wireless Components Letters*, Vol. 10, no. 7, Jul. (2000).
- [2] D. M. Pozar, “*Microwave Engineering*”, John Wiley & Sons, Inc., 3rd Edition, (2005).
- [3] Tasos Vayonakis, private communication.
- [4] Carlisle Plastics Company, Inc., 320 South Ohio Avenue, New Carlisle, OH 45344, USA.
- [5] Microwave Office, Applied Wave Research Inc. El Segundo, CA 90245, USA.
- [6] D. Koller, A. R. Kerr, and G. A. Ediss, “Proposed Quartz Vacuum Window Designs for ALAM bands 3 - 10”, NRAO, Charlottesville, VA [Online]. Available: <http://www.alma.nrao.edu/memos/html-memos/alma397/memo397.pdf>
- [7] P. F. Goldsmith, *Quasioptical Systems (IEEE)*, New York, (1998), Chap. 5.

